Li *et al.*
Chinese Journal of Mechanical Engineering (2022) 35:28
https://doi.org/10.1186/s10033-022-00705-4

Chinese Journal of Mechanical Engineering

ORIGINAL ARTICLE

Open Access

Step-by-Step Numerical Prediction of Aerodynamic Noise Generated by High Speed Trains

Tian Li*, Deng Qin, Ning Zhou and Weihua Zhang

Abstract

In this paper, the unsteady flow around a high-speed train is numerically simulated by detached eddy simulation method (DES), and the far-field noise is predicted using the Ffowcs Williams-Hawkings (FW-H) acoustic model. The reliability of the numerical calculation is verified by wind tunnel experiments. The superposition relationship between the far-field radiated noise of the local aerodynamic noise sources of the high-speed train and the whole noise source is analyzed. Since the aerodynamic noise of high-speed trains is derived from its different components, a stepwise calculation method is proposed to predict the aerodynamic noise of high-speed trains. The results show that the local noise sources of high-speed trains and the whole noise source conform to the principle of sound source energy superposition. Using the head, middle and tail cars of the high-speed train as noise sources, different numerical models are established to obtain the far-field radiated noise of each aerodynamic noise source. The far-field total noise of high-speed trains is predicted using sound source superposition. A step-by-step calculation of each local aerodynamic noise source is used to obtain the superimposed value of the far-field noise. This is consistent with the far-field noise of the whole train model's aerodynamic noise. The averaged sound pressure level of the far-field longitudinal noise measurement points differs by 1.92 dBA. The step-by-step numerical prediction method of aerodynamic noise of high-speed trains can provide a reference for the numerical prediction of aerodynamic noise generated by long marshalling high-speed trains.

Keywords: High-speed train, Aerodynamic noise, Sound source superposition, Numerical prediction

1 Introduction

As a high-speed train's running speed increases, the problem of aerodynamic noise will become more significant. When the train's running speed exceeds 300 km/h, aerodynamic noise will become the main source of high-speed train noise and impair further speed-up [1–5]. Therefore, noise reduction has become an important consideration in the design of high-speed trains. It is important to predict the aerodynamic noise of high-speed trains. Research methods for aerodynamic and acoustic behaviors of high-speed trains include full-scale experiment, wind tunnel experiment and numerical simulation. Current researchers have conducted extensive and in-depth researches, mainly on the identification of aerodynamic noise sources of high-speed trains, the mechanisms and characteristics of main noise sources, and optimization of noise sources [6–9].

In terms of experiments, Kitagawa and Nagakura [10] conducted a wind tunnel noise test on the Shinkansen high-speed train in Japan, and used acoustic array technology to identify the aerodynamic noise source of the high-speed train. At the same time, numerical calculations for the high-speed train are performed. The results show that the main sources of aerodynamic noise for high-speed trains include the pantograph, bogie, and air conditioner. Noh et al. [11] conducted a wind tunnel test

*Correspondence: litian2008@home.swjtu.edu.cn
State Key Laboratory of Traction Power, Southwest Jiaotong University, Chengdu 610031, China

on a 10-marshalling high-speed train model and identified the aerodynamic noise sources of the high-speed train. The results showed that the nose of the head car, bogies, pantographs, and windshields are the main aerodynamic noise source components of high-speed trains. Fremion et al. [12] conducted a full-scale test on a French TGV train and determined the location of aerodynamic noise sources to be in the bogie and pantograph regions. Lauterbach et al. [13] conducted an aerodynamic noise wind tunnel test on a 1/25th scale ICE3 high-speed train, and analyzed the characteristics of aerodynamic noise sources in the bogie region. Existing researches have demonstrated that the main sources of aerodynamic noise of high-speed trains are: the first bogie, pantographs, windshields, plough, air conditioner, head and tail cars, and the bogie skirt boards.

Numerical simulation is commonly used due to its low cost and short cycle time. Numerical simulation methods have been widely used to study the mechanical characteristics of the main noise sources of high-speed trains and optimize the noise sources. Zhu et al. [14] used DES and FW-H acoustic models to numerically simulate the flow field and far-field noise around high-speed trains. The results show that the aerodynamic noise of high-speed trains has wide frequency characteristics and that the first bogie of the high-speed train is the main aerodynamic noise source. Sassa et al. [15] used large eddy simulation (LES) and boundary element method (BEM) to numerically simulate the far-field aerodynamic noise of high-speed train doors, in a two-dimensional coordinate system. Sun et al. [16] studied the flow field and aerodynamic noise characteristics of high-speed train pantographs. The results show that the strips, balance rods, panhead, insulators, and frames are the main sources of aerodynamic noise generated from the pantograph. The radiated energy of the pantograph is mainly concentrated in the intermediate and high frequency bands. In the high frequency band, the far-field aerodynamic noise of the pantograph is mainly caused by the panhead. Zhang et al. [17, 18] used LES and Lighthill acoustic analogy theory to numerically simulate the aerodynamic noise of high-speed train motor and trailer bogies. The focus of the research was to analyze the noise directivity, attenuation and amplitude characteristics of the bogie. To date, many effective measures for noise reduction of the major noise sources of high-speed trains have been proposed after using numerical simulation technology, such as increasing the length of the streamline nose of the head car, installing skirt boards outside the bogie, and installing windshields in the inter-car gap region [19–21].

Looking at current research, due to complexity, the calculation of aerodynamic noise for full-size high-speed trains is difficult. The above research mainly emphasizes the aerodynamic noise of a certain part of the high-speed train, while research on the aerodynamic noise of the whole of the high-speed train is less common. An actual train is usually 8-marshalling and 16-marshalling. In the current numerical simulation, a simplified 3-marshalling train model is used. Although this can reduce the grid number, it cannot evaluate the far-field aerodynamic noise of a real long-marshalling train. Therefore, it's important to study the numerical prediction of aerodynamic noise of high-speed trains, based on the existing results.

In this paper, a certain type of 3-marshalling high-speed train is taken as the research object. By establishing different numerical models, the far-field noise of different parts is step-by-step obtained. Based on the superposition principle of aerodynamic noise sources of high-speed trains, the superimposed value of the far-field noise of each local aerodynamic noise source is obtained, which is used to predict the far-field aerodynamic noise of a long-marshalling high-speed train.

2 Numerical Methodology

2.1 Detached Eddy Simulation

LES and DES methods have been adopted by scholars to find aerodynamic noise sources in the near field of high-speed trains [22–25]. The basic idea of the LES method is to accurately solve the motion of all turbulent scales above a certain scale, and find the large-scale effects and pseudo-ordered structures that occur in many unsteady and non-equilibrium processes, which Reynolds Average Navier-Stokes (RANS) method cannot. Due to the high cost of calculation, LES method is rarely used in engineering. The DES method is a hybrid method, using the different characteristics of RANS and LES methods. LES method generally requires a dense grid in the boundary layer, while RANS method can use a relatively coarse grid in the near-wall area, while ensuring a certain degree of accuracy. Therefore, using RANS method in the boundary layer and LES method in the remaining regions can not only significantly reduce the grid number, but also maintain a high calculation accuracy. At present, DES method has also been successfully applied to the numerical simulation of flow around high-speed trains [26–29]. There are two widely used types of DES model. One is based on Spalart-Allmaras model. The other is based on SST k-ω model. In this study, we use the latter [30].

2.2 Acoustic Analogy

The acoustic analogy theory was originally proposed by Lighthill [31], and generalized by Ffowcs-Williams and Hawkings. The FW-H equation [32] is expressed as

$$\frac{1}{c_0^2}\frac{\partial^2 p'}{\partial t^2}-\nabla^2 p'=\frac{\partial}{\partial t}\left\{[\rho_0 v_n+\rho(u_n-v_n)]\delta(f)\right\}-\frac{\partial}{\partial x_i}\left\{[p_{ij}n_j+\rho u_i(u_n-v_n)]\delta(f)\right\}+\frac{\partial^2(T_{ij}H)}{\partial x_i x_j},\tag{1}$$

where p' is the sound pressure at the far field, c_0 is the sound speed, u_n is the fluid velocity component normal to the surface, v_n is the surface velocity component normal to the surface, n_j is the normal unit vector of the integral surface, $T_{ij}=\rho u_i u_j+\left(p'-c_0^2\rho'\right)\delta_{ij}-\tau_{ij}$ is the quadrupole noise source term generated by turbulence and vortices in the flow field, $\tau_{ij}=\mu\left(\partial u_i/\partial x_j+\partial u_j/\partial x_i\right)-2/3(\mu(\partial u_k/\partial x_k)\delta_{ij})$ is the viscous stress tensor, $\delta(f)$ is the Dirac delta function, $H(f)$ is the Heaviside function, $\nabla^2=\Delta$ is the Laplace operator.

The three terms on the right of the FW-H equation are the monopole, dipole, and quadrupole noise source terms respectively. For a running high-speed train, deformation of the train body can be ignored. Therefore, the surface of the train body can be regarded as a rigid body, the mass pulsation is almost zero, and the monopole sound source term can be ignored. The ratio of the intensity of the quadrupole source to the dipole source in the flow field is proportional to the square of Mach number. The noise intensity of the quadrupole source of high-speed trains is much smaller than that of the dipole source when the running speed is not larger than 350 km/h, therefore, the quadrupole source can also be ignored [33]. In this paper, only the far-field aerodynamic noise caused by the dipole sound source is investigated.

2.3 Sound Pressure Level

The aerodynamic noise of a high-speed train is obtained by superimposing the radiated noise of noise source components, such as the car body, pantograph, bogie, windshield, etc. Noise superposition follows the principle of square addition of sound pressure amplitude. Suppose that the effective sound pressure generated by the noise sources at the measuring point i is p_i , the square of the combined effective sound pressure p is expressed as

$$p^2=\sum_i^n p_i^2,\tag{2}$$

where n is the number of noise sources.

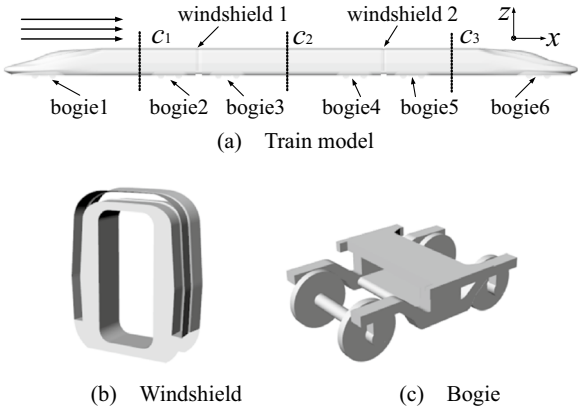

Figure 1 Geometric model

The sound pressure level SPL is defined as

$$SPL=10\sum_{i=1}^{n}\frac{p_i^2}{p_{\text{ref}}^2},\tag{3}$$

where p_{ref} is the reference sound pressure, and its value is 2×10^{-5} Pa.

According to the equation $p_i=p_{\text{ref}}\times10^{SPL_i/20}$, the superposition equation of sound pressure level can be obtained from Eqs. (2) and (3) and expressed as

$$SPL=10\lg\sum_{i=1}^{n}10^{0.1SPL_i}.\tag{4}$$

In real situations, aerodynamic noise is generated by multiple noise sources. By studying a single noise source component, the aerodynamic noise characteristics of the noise source component can be qualitatively analyzed. After this, a series of noise reduction measures can be carried out upon it.

The aerodynamic drag force coefficient C_{d} and pressure coefficient C_{p} are defined as

$$C_{\text{d}}=\frac{\boldsymbol{F}_{\text{d}}}{0.5\rho\boldsymbol{u}_\infty^2 A},\tag{5}$$

$$C_{\text{p}}=\frac{P_{\text{s}}}{0.5\rho\boldsymbol{u}_\infty^2},\tag{6}$$

where $\boldsymbol{u}_\infty$ is the incoming flow velocity, $\boldsymbol{F}_{\text{d}}$ is the aerodynamic drag forces, ρ is the air density, P_{s} is the static pressure; A is the characterized area of the high-speed train.

3 Numerical Model

3.1 Computational Model

A 3-marshalling train model composed of a head car, a middle car, a tail car, two windshields and six bogies is

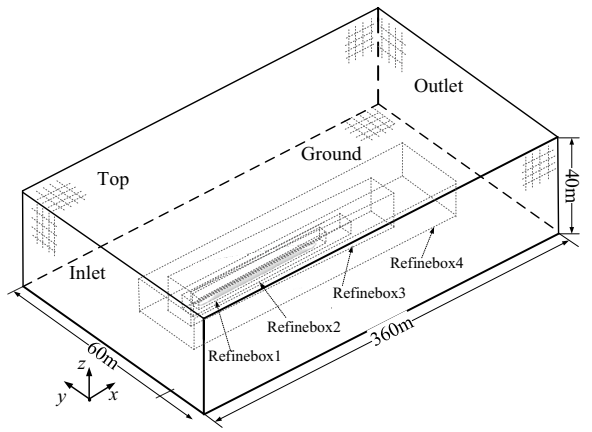

Figure 2 Computational domain

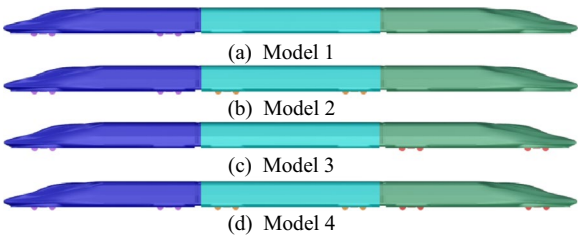

Figure 3 Simplified train geometric model

used in this study. As shown in Figure 1, length of the train is L=78.4 m, width W=2.9 m, height H=3.6 m, and the cross-sectional area of the car body A=9.84 m^2.

For the convenience of follow-up research, the head car body (including windshield 1), bogie 1 and bogie 2 are referred to as the head car. The middle car body, bogie 3 and bogie 4 are the middle car. The tail car body (including windshield 2), bogie 5 and bogie 6 are the tail.

In order to balance the relationship between numerical simulation accuracy and processing speed, an appropriate calculation domain is selected, as shown in Figure 2. The length, width and height of the calculation domain are 360 m, 60 m and 40 m respectively. The inlet surface of the calculation domain is about 80 m from the nose tip of the head car, the outlet surface is about 200 m from the nose tip of the tail car, the distance between the two sides and the track centerline is 30 m, and the bottom of the high-speed train is 0.376 m above from the ground.

The inlet boundary is set as the velocity inlet condition, and the speed is set at 350 km/h. The outlet boundary is specified as the pressure outlet condition with a 0 Pa gauge pressure. The right, left and top sides are symmetric boundaries. The train surface is set as the fixed wall. The ground is set as a slip wall with slip speed equal to the train's running speed, in the opposite direction.

3.2 Aerodynamic Noise Numerical Prediction Method

Although it is now possible to carry out the numerical calculation of the aerodynamic noise of an entire 3-marshalling high-speed train, the numerical calculation is still large, the calculation cycle is relatively long, and the entirety of the work can only be completed on high-performance computers. A step-by-step calculation method can be used to split a numerical calculation condition with a large number of grids into several calculation conditions, with a smaller number of grids, so as to more quickly calculate aerodynamic noise of the whole train.

To reduce the grid number when considering different aerodynamic noise source components, different simplified train models are selected to solve the local noise source, as shown in Figure 3. As the flow will affect the sound field, the flow around the aerodynamic noise source component calculated using the simplified model should be similar to one obtained using the whole train model. Therefore, a large error will not occur when solving a near-field noise source for a component. The geometric characteristics of the train model used in this paper are shown in Table 1. Model 4 is a 3-marshalling whole train. Models 1, 2 and 3 are simplified models based on Model 4.

3.3 Sound Measuring Points and Evaluation Criteria

In this paper, SST k-ω turbulence model and DES method are used to solve the steady and unsteady flow fields around the high-speed train, respectively. The far-field noise is solved using the FW-H acoustic analogy equation. The time steps of unsteady flow field and acoustic calculation are both 1×10^{-4} s and the physical simulation time of aerodynamic noise is 0.3 s. The maximum solvable frequency and frequency resolutions are 5 kHz and 3.3 Hz, respectively.

In order to analyze the characteristics of pulsating pressure on the surface of high-speed trains and the characteristics of far-field aerodynamic noise, multiple measuring points are arranged on and around the train surface, as shown in Figure 4. Three surface pressure measuring points are arranged on the roof of the longitudinal center section of the train. The arrangement of far-field acoustic measuring points for

Table 1 Model characteristics

Number	Geometric features	Aerodynamic noise source
Model 1	Without bogies 3, 4, 5, 6	Head
Model 2	Without bogies 5, 6	Middle
Model 3	Without bogies 2, 3, 4	Tail
Model 4	Whole train model	All parts

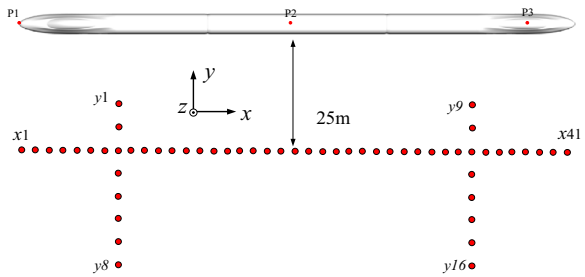

Figure 4 Schematic diagram of noise measurement point layout

high-speed trains is based on the standard ISO3095-2013 [34]. At a height of 3.5 m above the ground and 25 m away from the track centerline, 41 noise measurement points are evenly arranged along the longitudinal direction of the train. The distance between adjacent noise measurement points is 2 m. The longitudinal measuring points are numbered $x1$ to $x41$. The $x1$ noise measuring point corresponds to the position of the nose tip of the head car. At a height of 3.5 m above the ground, 16 noise measurement points are arranged horizontally across the train at 15 m, 20 m, 25 m, 30 m, 35 m, 40 m, 45 m, and 50 m. These measurement points are numbered $y1$ to $y16$.

According to the definition of ISO3095-2013, the equivalent continuous A-weighted sound pressure level can be used for the study of aerodynamic noise of high-speed trains. The expression is

$$SPL_{\mathrm{A}} = 10\lg\left(\frac{1}{T}\int_0^T \frac{p_{\mathrm{A}}^2(t)}{p_0^2}\mathrm{d}t\right), \tag{7}$$

where T is the total time interval, $p_A(t)$ represents the instantaneous A-weighted sound pressure.

When using a single noise measuring point, it is difficult to evaluate the aerodynamic noise characteristics of the whole train. Based on the principle of energy superposition, the average sound pressure level can be used as another indicator in aerodynamic noise evaluation, and its expression is

$$SPL_{p\mathrm{m}} = 10\lg\left(\frac{1}{m}\sum_{i=1}^{m} 10^{0.1(SPL_{p\mathrm{A}})_i}\right), \tag{8}$$

where $(SPL_{PA})_i$, $(i = 1, 2, 3..., m)$ is the equivalent continuous A-weighted sound pressure level of the i th noise evaluation point, and m is the total number of noise evaluation points.

3.4 Meshing Strategy

In order to verify grid independence, Model 4 is selected as the research object. Coarse, medium and fine grids are established using different grid refinement strategies. The total number of grid cells is 37.85 million, 48.21 million and 56.23 million, respectively. The average aerodynamic drag coefficient of the train and the sound pressure level at far-field noise measurement point $x8$ are chosen for comparison. It can be seen from Table 2 that the difference between the results obtained by using the medium and fine grid is relatively small. Therefore, a medium grid was selected for further research.

Table 2 Mesh independence

Level	Total cells (million)	C_d	Difference (%)	*SPL* (dBA)	Difference (dBA)
Coarse	37.85	0.297	–	93.2	–
Medium	48.21	0.303	2.02	93.8	0.6
Fine	56.23	0.300	− 0.99	93.6	− 0.2

Figure 5 Surface meshing of Model 1

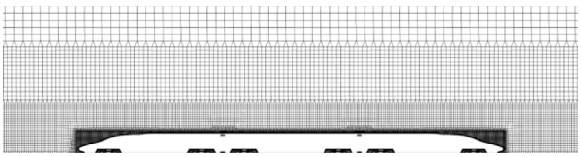

(a) Mesh on a cross-section

(b) Boundary layer grid

Figure 6 Meshing of Model 4

In order to further reduce the grid number, different meshing strategies are adopted for different high-speed train geometric models. Fine meshes are applied to the surface of aerodynamic noise source components. Rough meshes are applied to surfaces that are not a source of aerodynamic noise. Figure 5 shows the mesh of Model 1. When the head car is used as a source of aerodynamic noise, the surface grid of the head car is very fine. However, as the non-aerodynamic noise source components, the middle and tail cars have relatively rough surface meshes. It is worth noting that the streamlined parts of the train, bogie skirts and windshields have larger surface curvatures, and the grid is finer than in the other surfaces.

Figure 6 shows the mesh of Model 4. When the whole train is used as a source of aerodynamic noise, the head car, middle car, and tail car all have very fine meshes. In order to simulate the boundary layer flow near the train surface, a boundary layer grid is also generated, as shown in Figure 6(b). The height of the first layer of the boundary layer is 0.1 mm and the growth rate is 1.1, for a total of 14 layers. For different train models, the grid number is shown in Table 3. It can be seen that the meshing strategy in this study can significantly reduce the grid number.

4 Validation

An aerodynamic noise test of a high-speed train was conducted in the acoustic wind tunnel of the Low Speed Aerodynamics Research Institute of the China Aerodynamics Research and Development Center [35]. The test wind tunnel is a single-return low-turbulence acoustic wind tunnel. The cross section of the wind tunnel is 5.5 m wide and 4 m high, with the test section being 14 m long. The maximum wind speed at the opening test section of the wind tunnel is 100 m/s. The background noise of the opening test section is 75.6 dBA (at a lateral distance of 7.95 m from the center of the nozzle outlet, the cut-off frequency is 200 Hz, and the wind speed is 80 m/s).

The test uses a train model with a model scale of 1:8, as shown in Figure 7. In order to measure the far-field noise radiation characteristics of the test model, 30 far-field microphones were arranged on the side of the model. The far-field microphones are arranged vertically in 3 rows with a vertical spacing of 0.2 m. There are 10 in each row, with an axial spacing of 0.8 m. The detailed layout of the far-field microphones is shown in Figure 8.

A numerical simulation in the same configuration as the wind tunnel test is calculated. Taking the arithmetic average of the sound pressure level at the 30 noise measurement points, the comparison between the numerical calculation and the wind tunnel test is shown in Table 4. The differences between the wind tunnel results and the numerical results at different wind speeds are less than 1.5 dBA.

5 Results

The calculation results will be compared and analyzed in terms of aerodynamic force, flow field, far-field noise and frequency spectrum characteristics.

Table 3 Number of grids

	Model 1	Model 2	Model 3	Model 4
Cells Number (million)	34.58	29.25	36.74	56.23

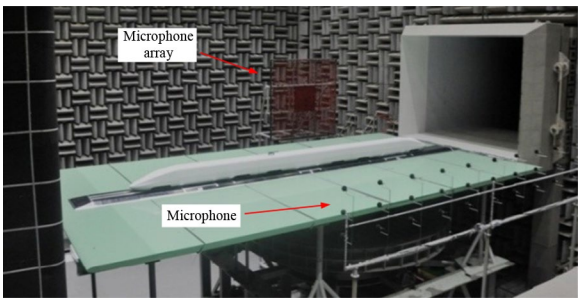

Figure 7 Wind tunnel experimental model

5.1 Sound Source Superposition

Based on Model 4, the sound source superposition principle of high-speed trains is studied by calculating the far-field aerodynamic noise of a single bogie, all six bogies, the body of the head car (BHC), the body of the middle car (BMC), the body of the tail car (BTC) and the whole car body (WCB). These are then considered as noise sources.

Figure 9 shows the far-field radiated noise of each bogie and all six bogies combined, at the noise monitoring point. According to Eq. (4), the "bogie synthesis" curve can be obtained. The results show that the radiated noise of bogie 1 in the far field is significantly greater than that of other bogies, and each bogie produces a local maximum sound pressure level at the corresponding noise monitoring point. In general, the radiated noise of the 6 bogies to the far field gradually decreases from the front to the rear. The sound pressure level curve of the "bogie synthesis" is similar to all bogies combined, as a noise source. It shows that the sound source of the bogies conforms to the principle of noise superposition.

Figure 10 shows the far-field sound pressure level curves of different parts of both the car body and the whole car body. The maximum sound pressure level of the head car area is at the $x8$ noise measurement point, which corresponds to the streamline transition position of the head car. The maximum

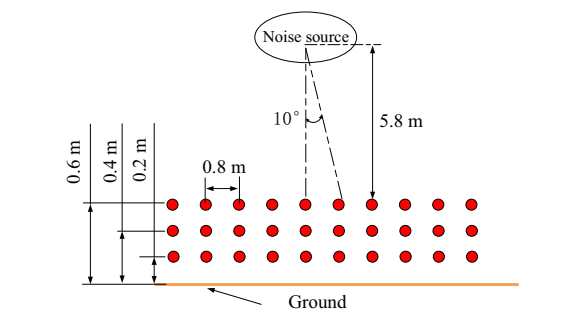

Figure 8 Schematic diagram of far-field microphones

Table 4 Comparison of numerical simulation and wind tunnel test

Model state	Wind speed(km/h)	Experiment(dBA)	CFD(dBA)	Error(dBA)
Without pantograph	160	72.70	71.48	−1.22
	200	79.09	78.03	−1.26
	250	85.95	84.63	−1.32

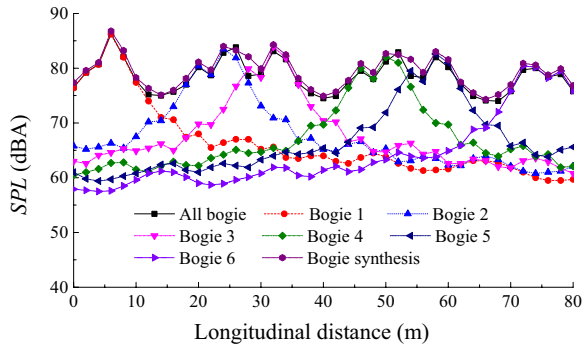

Figure 9 Far-field noise analysis of the bogie

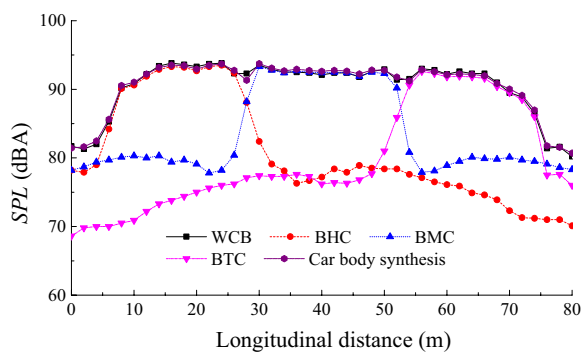

Figure 10 Far-field noise analysis of the car body

sound pressure level of the tail car appears at the $x34$ noise measurement point, which corresponds to the streamline transition position of the tail car. Overall, the radiated noise of the head car is greater than that of the tail car, and the maximum sound pressure level appears in the head car. This indicates that the head car is the main source of aerodynamic noise. According to Eq. (4), the radiated noise from different parts of the car body at the noise measuring points can be used as the "car body synthesis" sound pressure level curve. The sound pressure level curve for "car body synthesis" is similar to that for all car bodies being used as noise sources. This demonstrates that the noise sources of the car body also conform to the principle of sound source superposition.

Table 5 Time-averaged aerodynamic drag coefficients of different geometric train models

Part	Geometry			
	Model 1	Model 2	Model 3	Model 4
Head	0.158	0.156	0.140	0.162
Middle	0.055	0.061	0.054	0.063
Tail	0.069	0.067	0.080	0.076
All	0.282	0.284	0.274	0.300

5.2 Aerodynamic

Table 5 shows the comparison results of the aerodynamic drag coefficients of the four train models. As some bogies are neglected in Model 1, Model 2 and Model 3, their time-averaged aerodynamic drag coefficients are smaller with comparison to Model 4. The differences are 2.5 %, 3.2 % and 5.3 %, respectively. The aerodynamic drag of high-speed trains is mainly composed of differential pressure resistance and viscous resistance. Most of the viscous resistance comes from the car body. With the bogie being removed, there is little effect on the surface viscous resistance of the train, but there is a greater effect on the pressure resistance of the front and rear of the train. It can be seen from Table 4 that due to of the neglection of bogies 2, 3, and 4 in Model 3, a large amount of airflow moving into the rear of the train will cause an increase in the pressure resistance of the tail car.

Figure 11 shows the pressure coefficient time-history curves of the measurement points P1, P2 and P3 for different high-speed train models. It can be seen from the figure that for all models, the time-average pressure coefficient of the stagnation point P1 is close to 1, and the difference between the time-averaged pressure coefficients of the monitoring points P2 and P3 is very small. The results show that the difference in the underbody structures has little effect on the flow above the roof.

Figure 12 shows more comparison results of the pressure coefficients of the cross sections at different parts of the train. The cross section positions are shown in Figure 1.

It can be seen from Figure 12 that the time-averaged pressure coefficient curves of Model 1 and Model 4 at the cross-section c_1 are broadly in agreement. The flow field in the front of the train is less affected by the rear

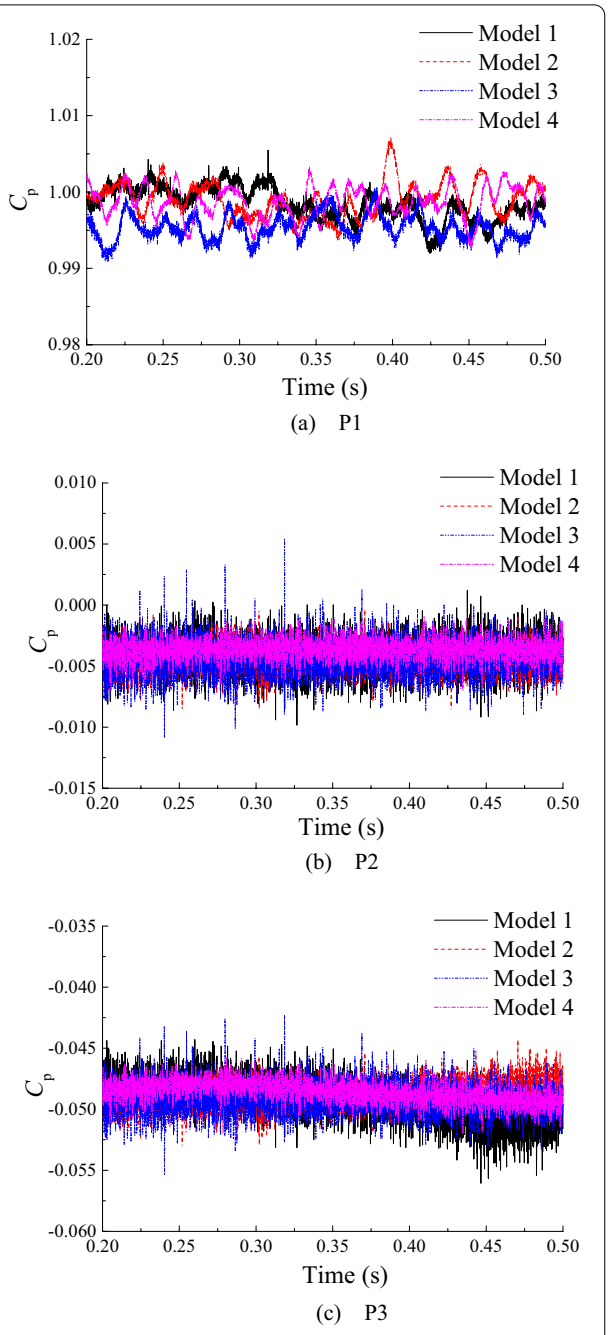

Figure 11 Time history curves of pressure coefficient at surface measuring points

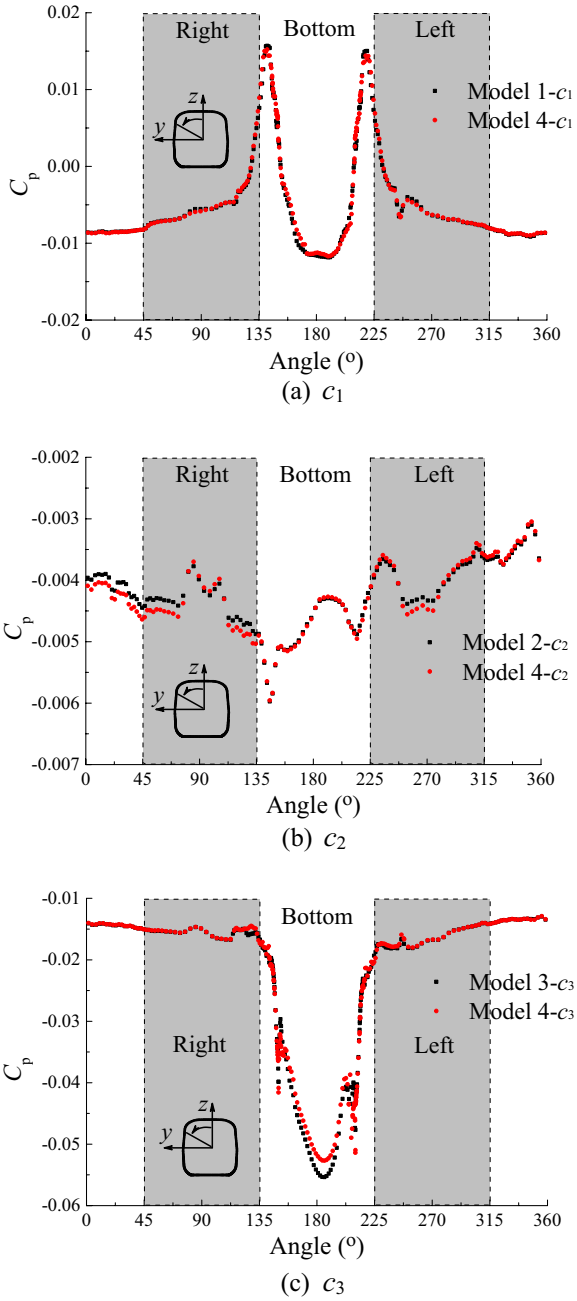

Figure 12 Comparison of time-averaged pressure coefficients for different cross-sections of car bodies

structure. The time-averaged pressure coefficient curves of Model 2 and Model 4 at cross-section c_2 also agree well. Due to the difference in the mesh of the head car, the flow field around the middle car will be affected to a certain extent, and the time-averaged pressure coefficient on the surface will be different. Model 3 and Model 4 have the same time-averaged pressure coefficient distribution at the cross-section c_3. However, the time-averaged pressure coefficient varies significantly underneath the train. The main reason is that Model 3 ignores bogies 2, 3 and 4, which leads to a weaker blockage of the airflow underneath the train. This leads to a higher airflow velocity and greater negative pressure at the bottom. In summary, Models 1, 2, and 3 are simplified forms of

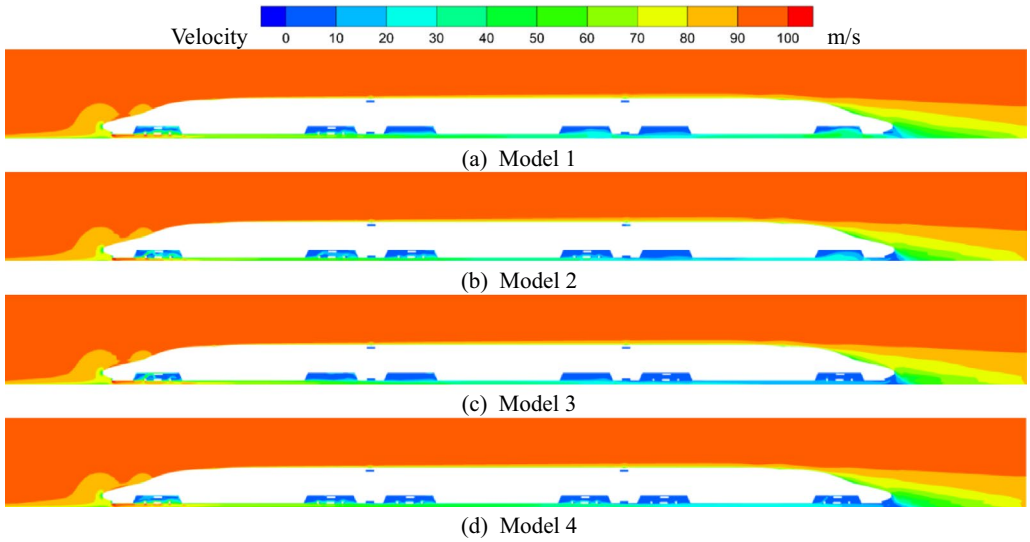

Figure 13 Time-averaged velocity distribution in the longitudinal center section

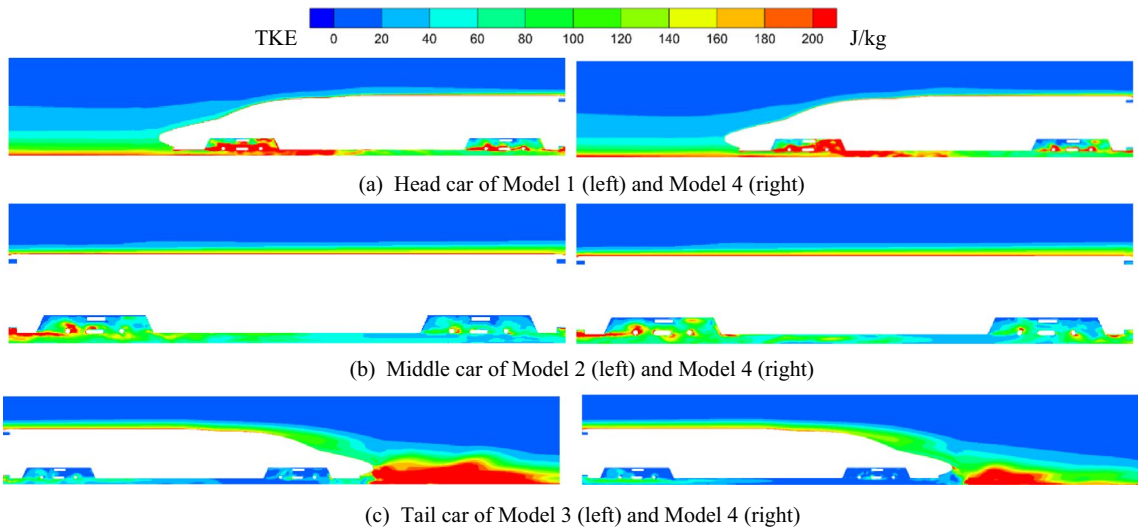

Figure 14 Comparison of TKE

Model 4, whose simplifications do not cause a significant change in the pressure distribution on the train. There is reasonable similarity between them.

5.3 Flow Field

Aerodynamic noise is the result of the interaction between fluid and structure as the air flows over a solid surface. The similarity of the flow field implies a similarity of sound field.

Figure 13 shows the time-averaged speed distribution of the longitudinal central cross-section of the train for different train models. It can be seen from the figure that the flow fields around simplified Models 1, 2, and 3 have a certain degree of similarity to the flow fields around Model 4. When the head car or the middle car is used as the aerodynamic noise source, the velocity field distribution around the noise source is basically the same. When the tail car is used as the source of aerodynamic noise, compared with Model 4, Model 3 has a different velocity field distribution around the tail car. This is the result of Model 3 ignoring several bogies.

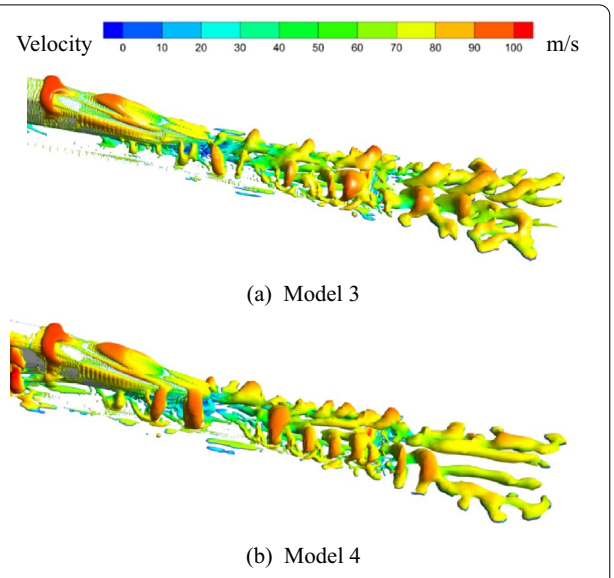

Figure 15 Comparison of wake vortex structure (colored by velocity)

Figure 14 shows the distribution of turbulent kinetic energy in the longitudinal center section of the flow field calculated by Models 1, 2, 3 and 4. Turbulent kinetic energy (TKE) can describe the mixing ability of the turbulent flow field around the train. The aerodynamic noise distribution on the train surface can also be effectively evaluated, by analyzing the TKE. It can be seen from the figure that the bogie 1, head car and tail car wake regions have high TKE values, which are the main sources of aerodynamic noise. When the head, middle and tail cars are considered as aerodynamic noise sources, Models 1, 2 and 3 are devised, respectively. When the head car or the middle car are used as the aerodynamic noise source, the distribution of TKE around the noise source is almost the same. However, there are slight differences in some regions. When the tail car is used as the source of aerodynamic noise, Model 3 ignores multiple bogies resulting in a large increase in the TKE in the wake area of the tail car with comparison to Model 4.

Figure 15 shows the wake vortex structures of Model 3 and Model 4. The vortex structure around Model 3 has not changed substantially. However, the vortex scale and vorticity in some regions are different. Overall, the distribution of flow fields around the simplified model and the whole train model is quite similar.

5.4 Far-field Aerodynamic Noise

Figure 16 shows the sound pressure level distribution of the far-field longitudinal noise measurement points ($x1$–$x41$) for different train models. When the head, middle or tail cars are used as the sources of aerodynamic noise, the far-field noise distributions of Model 1, Model 2 and Model 3 are compared with Model 4, with which they

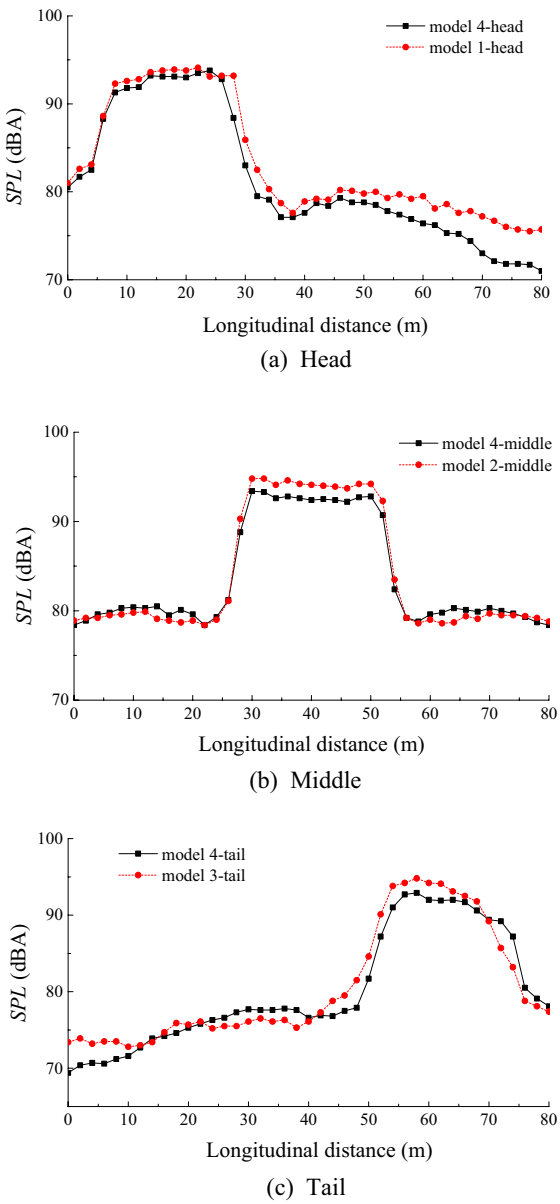

Figure 16 Sound pressure level of longitudinal noise measuring point ($x1$–$x41$)

are consistent. When the head car is used as the source of aerodynamic noise, both the noise distribution and SPL of the head car of Model 1 and Model 4 are almost the same. The flow field around the head is less affected, and the difference in sound pressure level at the noise measurement point ($x1$–$x15$) is smaller, with a maximum difference of 1.0 dBA. When the middle car is used as the aerodynamic noise source, due to the little influence of model simplification and meshing, the noise distributions of Model 2 and Model 4 at the far-field noise

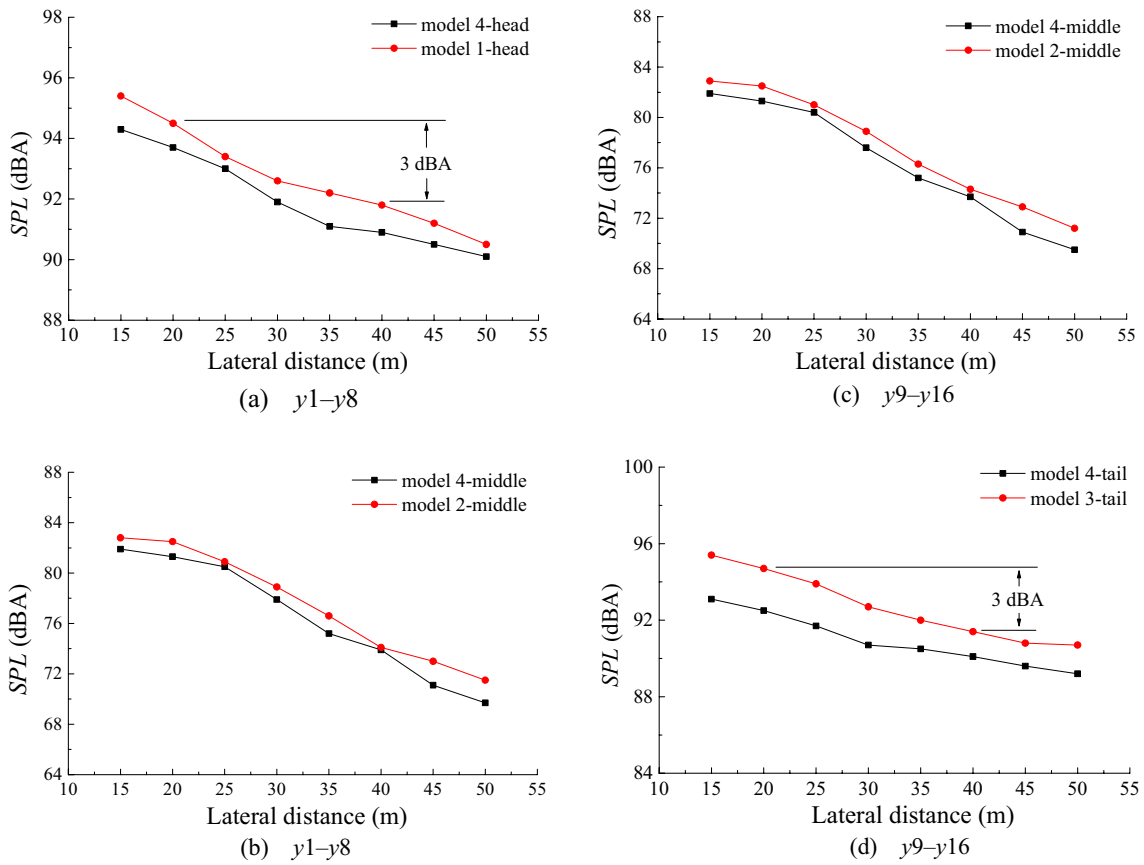

Figure 17 Sound pressure level curve of transverse noise measurement points (*y*1–*y*16)

measurement points (*x*14–*x*27) are basically the same. However, there is a slight difference in sound pressure level, the maximum difference being 1.8 dBA. When the tail car is used as the aerodynamic noise source, the air flow underneath the train is affected (as it ignores multiple bogies). The vortex flow field of Model 3 is more complicated. Compared with Model 4, the sound pressure level at the far-field noise measurement points (*x*27–*x*41) is larger, with a maximum difference of 3.6 dBA.

Figure 17 shows the sound pressure level distribution of the far-field lateral noise measurement points (*y*1–*y*16) for different train models. It can be seen from the figure that the sound pressure level distributions of the lateral noise evaluation points are quite similar for different models. As the distance increases, the sound pressure level of the noise measurement point gradually decreases. When the distance is doubled, the sound pressure level of the noise measuring point is reduced by approximately 3 dBA. When the head, middle or tail cars are used as the sources of aerodynamic noise, the sound pressure levels at the far-field noise measurement points of Model 1, Model 2 and Model 3 are each compared with Model 4, respectively. The maximum difference in sound pressure level between noise measurement points at the same location is 1.1 dBA, 2 dBA and 2.3 dBA, respectively.

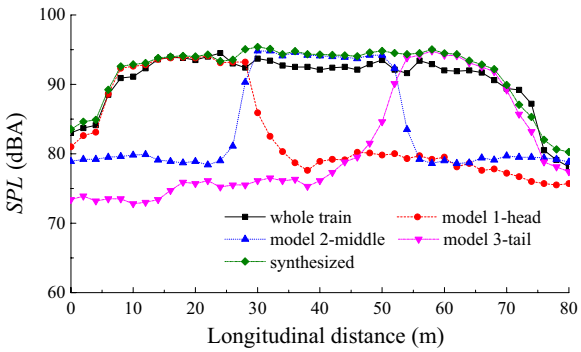

Figure 18 Superposition of sound pressure level at longitudinal noise measuring point

Figure 18 shows the superimposed results of the sound pressure levels of different high-speed train models at the longitudinal noise measurement points in the far field.

Table 6 Comparison of average sound pressure level

Calculation model	Average sound pressure level (dBA)	Error(dBA)
Model 4	91.80	–
Synthesis	93.72	— 1.92

Based on Model 1, Model 2 and Model 3, the far-field aerodynamic noises of head, middle and tail cars are calculated, respectively. The "synthesized" sound pressure level is then obtained based on the principle of sound source superposition. The "synthesized" sound pressure level curve is in good agreement with the far-field longitudinal noise distribution calculated by Model 4. The maximum difference in sound pressure level at the noise measurement point, at the same location, is 3.7 dBA.

Table 6 gives the average sound pressure level of $x1$–$x41$ noise measurement points. It can be seen that the average sound pressure level calculated by Model 4 is 91.8 dBA, and the average sound pressure level of the "synthesized" pressure level obtained using Models 1, 2, and 3, is 93.72 dBA. The difference between the two is 1.92 dBA. Based on the principle of superposition of sound sources, the error of numerically predicting the far-field aerodynamic noise of the whole train model using a stepwise calculation method of aerodynamic noise sources, is within an acceptable range.

5.5 Spectrum Characteristics

When using the head, middle and tail as the aerodynamic noise source, the power spectral density of the far-field noise measurement points ($x8$, $x21$ and $x34$) is calculated with different high-speed train models and shown in Figure 19. Figure 19(a), (b) and (c) shows the comparison results of the power spectral density of the simplified models (Model 1, Model 2, and Model 3), and the whole train model (Model 4). It can be seen from the figure that the aerodynamic noise of the high-speed train has no obvious dominant frequency, and the amplitude of the power spectral density of the noise measurement point at low frequencies is slight greater than that at high frequencies. The frequency information of the far-field noise measurement points calculated by using Models 1, 2, and 3 are close to the results calculated by using Model 4. It shows that a simple model can be used to calculate the far-field noise of a certain local aerodynamic noise source component, and it will not cause a large reduction in the total noise energy.

Figure 20 shows the equivalent continuous A-weighted 1/3 octave frequency of the far-field noise measurement points ($x8$, $x21$ and $x34$) for different train models. It can be seen from the figure that the far-field aerodynamic noise of a high-speed train is broadband noise. When a high-speed train runs at a speed of 350 km/h, the noise energy of the vehicle is mainly concentrated in the range of 800–4000 Hz. The 1/3 octave frequency of the far-field noise measurement point calculated by the simple model is similar to the result calculated by the whole train model. The far-field noise calculation of the local aerodynamic noise source using the simple model does not change the spectrum distribution law of the noise source.

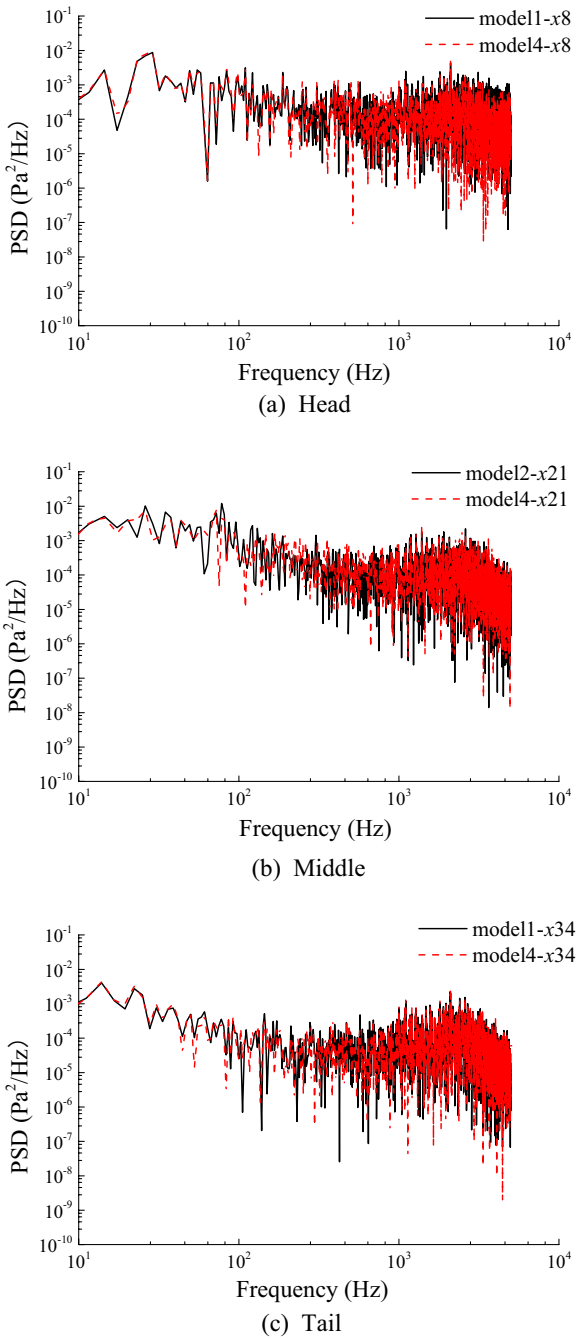

Figure 19 Power spectral density of different far-field noise measurement points

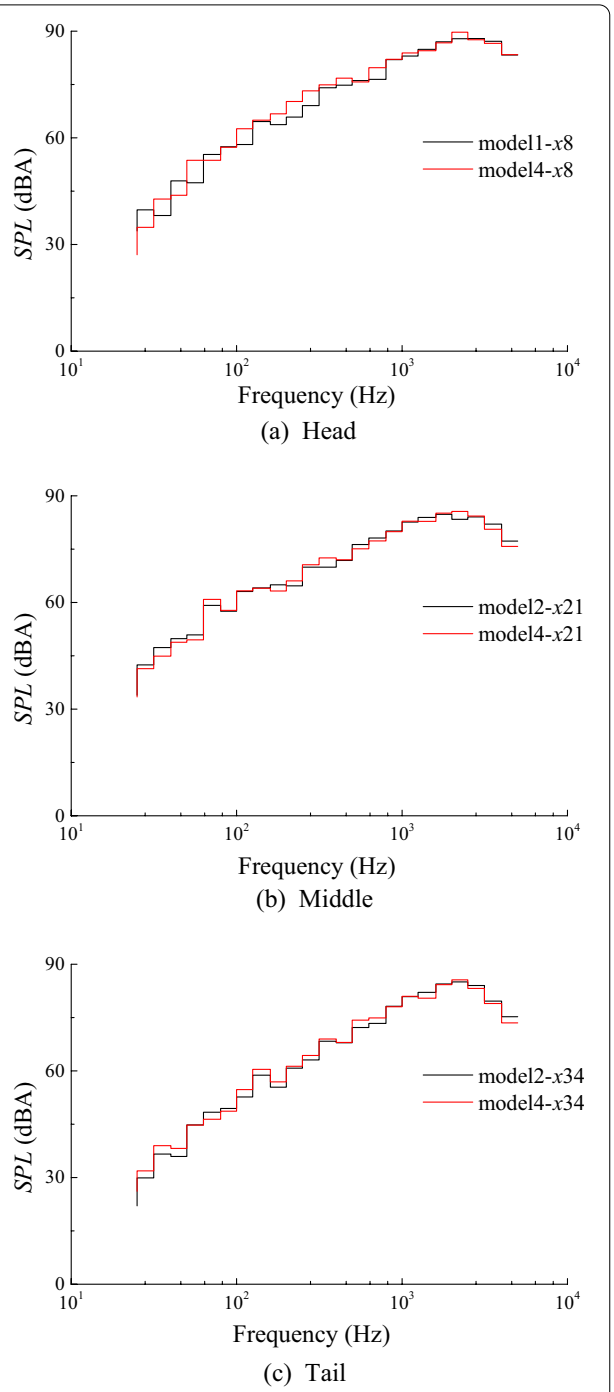

Figure 20 1/3 octave frequency of different far-field noise measurement points

6 Conclusions

In this study, the aerodynamic noise characteristics and numerical prediction methods of high-speed trains are investigated by means of numerical simulation. The reliability of numerical simulation and methods is verified by wind tunnel experiments. By comparing and analyzing the aerodynamic and aerodynamic noise characteristics of high-speed trains with different degrees of simplification, the following conclusions can be drawn:

(1) The whole noise source and all local noise sources of the high-speed train conform to the principle of energy superposition. The radiation noise of the head car to the far field is greater than that of the tail car. The far-field radiated noise of the first bogie of the head car is significantly greater than that of the other bogies.

(2) Compared with the time-averaged aerodynamic drag coefficients of the head, middle, and tail of the whole train model, the errors of the head car of Model 1, the middle car of Model 2 and the tail car of Model 3 are 2.5%, 3.2% and 5.3%, respectively. The simplified model does not significantly change the surface pressure distribution, flow field structure and aerodynamic noise source.

(3) The far-field noise sound pressure level and frequency spectrum information of specific local aerodynamic noise sources obtained by the simplified model are almost consistent with the results calculated by the whole train model. High-speed trains are composed of multiple main aerodynamic noise source components, which can be used to step-by-step predict the aerodynamic noise of different components. The method proposed in this paper can provide a reference for solving the aerodynamic noise of a long-marshalling high-speed train.

Acknowledgements
Not applicable.

Authors' contributions
TL was in charge of the whole trial and wrote the manuscript; DQ assisted with the post process of the data and analysis; NZ revised the manuscript and gave some advice; WZ proposed the idea and the model. All authors read and approved the final manuscript.

Authors' information
Tian Li, born in 1984, is currently an associate professor at *State Key Laboratory of Traction Power, Southwest Jiaotong University, China*. He received his doctor degree from *Southwest Jiaotong University, China*, in 2012. His research interests include train aerodynamics, and computational fluid dynamics.
Deng Qin, born in 1996, is currently a master candidate at *State Key Laboratory of Traction Power, Southwest Jiaotong University, China*.
Ning Zhou, born in 1977, is currently an associate professor at *State Key Laboratory of Traction Power, Southwest Jiaotong University, China*.
Weihua Zhang, born in 1961, is currently a professor at *State Key Laboratory of Traction Power, Southwest Jiaotong University, China*. His research interests include coupled system dynamics of high-speed train, and pantograph dynamics.

Funding
Supported by National Key Research and Development Program of China (Grant No. 2020YFA0710902) and National Natural Science Foundation of China (Grant No. 12172308).

Competing interests
The authors declare no competing financial interests.

Received: 14 September 2020 Revised: 13 January 2022 Accepted: 22 March 2022
Published online: 05 April 2022

References

[1] C Talotte. Aerodynamic noise: A critical survey. *Journal of Sound and Vibration*, 2000, 231(3): 549-562.
[2] J Zhang, X B Xiao, X Z Sheng, et al. Sound source localisation for a high-speed train and its transfer path to interior noise. *Chinese Journal of Mechanical Engineering*, 2019, 32(1): 59.
[3] T Li, Z Y Dai, M G Yu, et al. Numerical investigation on the aerodynamic resistances of double-unit trains with different gap lengths. *Engineering Applications of Computational Fluid Mechanics*, 2021, 15(1): 549-560.
[4] D J Thompson, E Latorre Iglesias, X W Liu, et al. Recent developments in the prediction and control of aerodynamic noise from high-speed trains. *International Journal of Rail Transportation*, 2015, 3(3): 119-150.
[5] J Zhang, X B Xiao, X Z Sheng, et al. Characteristics of interior noise of a Chinese high-speed train under a variety of conditions. *Journal of Zhejiang University SCIENCE A*, 2017, 18(8): 617-630.
[6] Z X Sun, J J Song, Y R An. Numerical simulation of aerodynamic noise generated by high speed trains. *Engineering Applications of Computational Fluid Mechanics*, 2012, 6(2): 173-185.
[7] K Nagakura. Localization of aerodynamic noise sources of Shinkansen trains. *Journal of Sound and Vibration*, 2006, 293(3-5): 547-556.
[8] D Qin, T Li, H L Wang, et al. A fast approach for predicting aerodynamic noise sources of high-speed train running in tunnel. *Computer Modeling in Engineering & Sciences*, 2022, 130(3): 1371-1386.
[9] Y F Yao, Z X Sun, G W Yang, et al. Analysis of aerodynamic noise characteristics of high-speed train pantograph with different installation bases. *Applied Science*, 2019: 1-21.
[10] T Kitagawa, K Nagakura. Aerodynamic noise generated by shinkansen cars. *Journal of Sound and Vibration*, 2000, 231(5): 913-924.
[11] H M Noh, S Choi, S Hong, et al. Investigation of noise sources in high-speed trains. *Proceedings of the Institution of Mechanical Engineers Part F-Journal of Rail and Rapid Transit*, 2014, 228(3): 307-322.
[12] N Fremion, N Vincent, M Jacob, et al. Aerodynamic noise radiated by the inter-coach spacing and the bogie of a high-speed train. *Journal of Sound and Vibration*, 2000, 231(3): 577-593.
[13] A Lauterbach, K Ehrenfried, S Loose, et al. Microphone array wind tunnel measurements of Reynolds number effects in high-speed train aeroacoustics. *International Journal of Aeroacoustics*, 2012, 3(11): 411.
[14] C L Zhu, H Hemida, D Flynn, et al. Numerical simulation of the slipstream and aeroacoustic field around a high-speed train. *Proceedings of the Institution of Mechanical Engineers Part F-Journal of Rail and Rapid Transit*, 2017, 231(6): 740-756.
[15] T Sassa, T Sato, S Yatsui. Numerical analysis of aerodynamic noise radiation from a high-speed train surface. *Journal of Sound and Vibration*, 2001, 247(3): 407-416.
[16] X Q Sun, H Xiao. Numerical modeling and investigation on aerodynamic noise characteristics of pantographs in high-speed trains. *Complexity*, 2018: 1-12.
[17] Y D Zhang, J Y Zhang, L Zhang, et al. Numerical analysis of aerodynamic noise of motor car bogie for high-speed trains. *Journal of Southwest Jiaotong University*, 2016, 51(5): 870–877. (in Chinese)
[18] Y D Zhang, J Y Zhang, T Li, et al. Numerical research on aerodynamic noise of trailer bogie. *Journal of Mechanical Engineering*, 2016, 52(16): 106-116. (in Chinese)
[19] H H Yu, J C Li, H Q Zhang. On aerodynamic noises radiated by the pantograph system of high-speed trains. *Acta Mechanica Sinica*, 2013, 29(3): 399–410.
[20] J M Wu. Numerical computation and improvement of aerodynamic radiation noises of pantographs. *Journal of Vibro-Engineering*, 2017, 19(5): 3939–3952.
[21] Y D Zhang, J Y Zhang, T LI, et al. Investigation of the aeroacoustic behavior and aerodynamic noise of a high-speed train pantograph. *Science China Technological Sciences*, 2017, 60(4): 561-575.
[22] C Y Yuan, M Q Li. Multi-objective optimization for the aerodynamic noise of the high-speed train in the near and far field base on the improved NSGA-II algorithm. *Journal of Vibro-Engineering*, 2017,19(6): 4759-4782.
[23] Y D Zhang, L Han, M Li, et al. Reduction of aerodynamic noise of high-speed train pantograph. *Journal of Mechanical Engineering*, 2017, 53(6): 94-101. (in Chinese)
[24] W T Lu, Y Wang, C Q Zhang. Research on the distribution of aerodynamic noises of high-speed trains. *Journal of Vibro-Engineering*, 2017, 19(2): 1438–1452.
[25] Y H Wang, J T Wang, L Q Fu. Numerical computation of aerodynamic noises of the high speed train with considering pantographs. *Journal of Vibro-Engineering*, 2016, 18(8): 5588-5604.
[26] H X Yang, D M Liu. Numerical study on the aerodynamic noise characteristics of CRH2 high-speed trains. *Journal of Vibro-Engineering*, 2017, 19(5): 3953-3967.
[27] T Li, Z Y Dai, W H Zhang. Effect of RANS model on the aerodynamic characteristics of a train in crosswind using DDES. *Computer Modeling in Engineering and Sciences*, 2020, 122(2): 555-570.
[28] Y F Cui, C Tian, Z Y Zhao. Research on the radiation characteristics of aerodynamic noises in the connection position of high-speed trains. *Journal of Vibroengineering*, 2017, 19(4): 3099-3112.
[29] T Li, H Hemida, J Y Zhang, et al. Comparisons of SST and DES simulations of the flow around trains. *Journal of Fluids Engineering*, 2018, 140(11): 111108-12.
[30] T Li, D Qin, W H Zhang, et al. Study on the aerodynamic noise characteristics of high-speed pantographs with different strip spacings. *Journal of Wind Engineering and Industrial Aerodynamics*, 2020, 202: 104191.
[31] M J Lighthill. On sound generated aerodynamically. I. General theory. *Proceedings of the Royal Society of London. Series A, Mathematical and Physical Sciences*, 1952, 211(1107): 564-587.
[32] J E Ffowcs-Williams, D L Hawkings. Sound generation by turbulence and surfaces in arbitrary motion. *Philosophical Transactions for the Royal Society of London. Series A, Mathematical and Physical Sciences*, 1969, 264(1151): 321-342.
[33] Z X Sun, D L Guo, S B Yao, et al. Identification and suppression of noise sources around high speed trains. *Engineering Applications of Computational Fluid Mechanics*, 2013, 7(1): 131-143.
[34] ISO, "Acoustics-railway applications-measurement of noise emitted by railbound vehicles," ISO 3095, 2013.
[35] Y D Zhang, J Y Zhang, T LI, et al. Research on aerodynamic noise reduction for high-speed trains. *Shock and Vibration*, 2016, 2016: 1-21.